X`Supplementary information for

"Field-free coexistence of skyrmions and anti-skyrmions induced by higher-order interactions and biaxial strain in NiI_2 monolayer"

Zebin Wu, Wenguang Hu, Liang Qiao* and Haiyan Xiao†

School of Physics, University of Electronic Science and Technology of China, Chengdu 611731, China.

Email: liang.qiao@uestc.edu.cn (L. Qiao*); hyxiao@uestc.edu.cn (H.Y. Xiao†)

I. Effect of strain on atomic structure of monolayer NiI_2

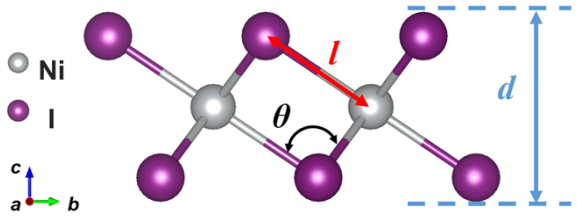

Fig. S1 Side view of the atomic structure of monolayer NiI_2. The thickness, ∠Ni-I- Ni bond angles and <Ni-I> bond length are denoted by d, θ and l, respectively.

Tab. S1. The lattice constant a (Å), thickness d (Å), ∠Ni-I-Ni bond angles θ (°) and <Ni-I> bond length l (Å) of monolayer NiI_2 under different strain ε (%) after complete structural relaxation.

ε(%)	a (Å)	d (Å)	θ (°)	l (Å)
-8	**3.667**	**3.291**	**86.283**	**2.682**
-6	**3.747**	**3.238**	**87.793**	**2.702**
-4	**3.827**	**3.185**	**89.265**	**2.723**
-2	**3.907**	**3.136**	**90.651**	**2.747**
0	**3.986**	**3.089**	**91.966**	**2.772**
2	**4.066**	**3.043**	**93.222**	**2.798**
4	**4.146**	**2.997**	**94.450**	**2.824**
6	**4.225**	**2.955**	**95.596**	**2.852**
8	**4.305**	**2.910**	**96.726**	**2.880**

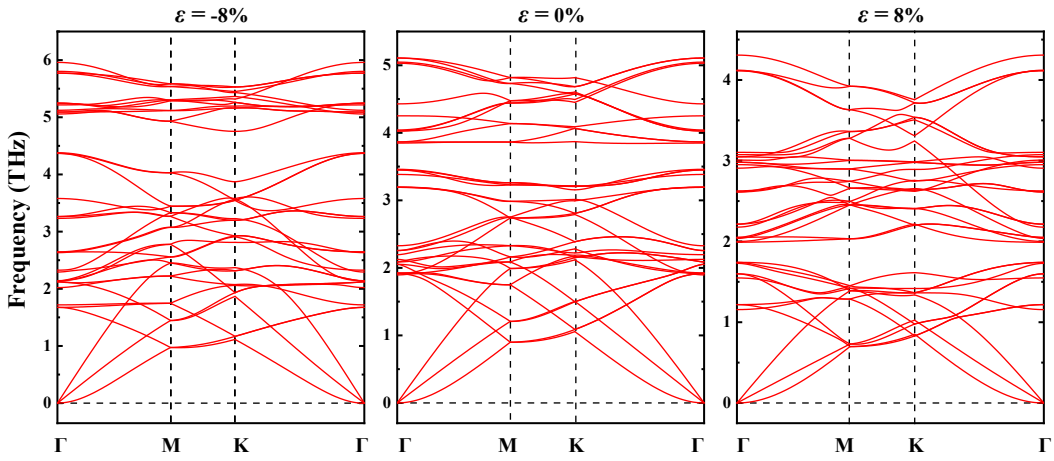

FIG. S2. The phonon dispersions for the monolayer NiI_2 at -8%, 0%, and +8% biaxial strain.

II. Calculation methods

A. Energy dispersion of spin spirals

Spin spirals are a representation of the general solution of the Heisenberg model on a periodic lattice. Such collective rotation of spins can be considered as a generalized translation action based on the generalized Bloch theorem (gBT)[1-3]. It is characterized by the spin spiral vector, denoted as q, which determines both the propagation direction of the spin spiral as well as the canting angle between two neighboring magnetic atoms. The magnetic moment M_i at an atomic position R_i is defined as $M_i = M\left(\cos\left(q \cdot R_i\right), \sin\left(q \cdot R_i\right), 0\right)$, where M_i represents the magnetic moment at lattice site R_i and q is the wave vector within the two-dimensional Brillouin zone (2DBZ)[4]. We select this vector along the high symmetry directions of the hexagonal 2DBZ, specifically the M-Γ-K-M directions. Each point within the BZ corresponds to a unique magnetic state, for example, the Γ point represents the FM state, the M point represents the row-wise AFM state, and the K point represents the Neel state with angles of 120° between adjacent magnetic atoms. The energies of spin spiral within the chemical unit cell are calculated by using gBT as implemented in the VASP package[5].

B. Atomistic spin dynamics simulations

Based on the Heisenberg model and Landau-Lifshitz-Gilbert (LLG) equation[6, 7], the micro-magnetic atomistic simulations are performed by VAMPIRE package[8]. To conduct simulations, a sample of ML-NiI_2 with dimensions of 55 nm × 55 nm is generated. In these simulations, only the lattice composed of magnetic atom is considered, while the nonmagnetic I atoms are ignored. Periodic boundary conditions are applied in the in-plane directions. This choice removes physical domain boundaries and eliminates artificial edge effects. All magnetic interaction parameters, including exchange interactions, magnetic anisotropy, and higher-order terms, are taken from first-principles calculations and implemented through the VAMPIRE material files. The spin dynamics are integrated using the Heun scheme for the LLG equation with a Gilbert damping constant of $\alpha = 0.1$ and a time step of 1×10^{-16} s. All simulations are conducted at zero temperature without thermal fluctuations. The spin system is initialized from random configurations and subsequently relaxed using the LLG dynamics until a stationary magnetic state is reached. A total of 5×10^6 time steps are employed to ensure convergence of the magnetic textures. When applied, the external magnetic field is oriented perpendicular to the monolayer plane.

III. Calculation of the spin Hamiltonian

To explore the magnetic properties of ML-NiI_2, an effective spin Hamiltonian is given as:

$$H = \frac{1}{2}\sum_{i,j} J_{ij}(S_i \cdot S_j) + A_i \sum_i \left(S_i^z\right)^2 + H_{HOIs} \#() \quad 1.$$

, where J_{ij} and A_i represent the Heisenberg exchange interactions of Ni atoms and single ion anisotropy, respectively. The last term H_{HOIs} represents the higher order interactions (HOIs). Arising from a multiple-electron hopping process between 2 to 4 atomic sites, the HOIs terms consist of two-sites-four-spin interaction, or biquadratic interaction B, three-sites-four-spin interaction Y, and four-sites-four-spin interaction F[9]:

$$H_{HOIs} = \frac{1}{2}B\sum_{i,j}(S_i \cdot S_j)^2 + Y\sum_{i,j,k}\left[(S_i \cdot S_j)(S_j \cdot S_k) + (S_j \cdot S_k)(S_k \cdot S_i) + (S_i \cdot S_k)(S_i \cdot S_j)\right] + \frac{1}{4}F\sum_{i,j,k,l}\left[(S_i \cdot S_j)(S_k \cdot S_l) + (S_i \cdot S_l)(S_j \cdot S_k) - (S_i \cdot S_k)(S_j \cdot S_l)\right] \#(). \quad 2.$$

Here, $\vec{S}_i$, $\vec{S}_j$, $\vec{S}_k$ and $\vec{S}_l$ are the spin vector of each magnetic atoms at site i, j, k and l, which are normalized to $|\vec{S}| = 1$.

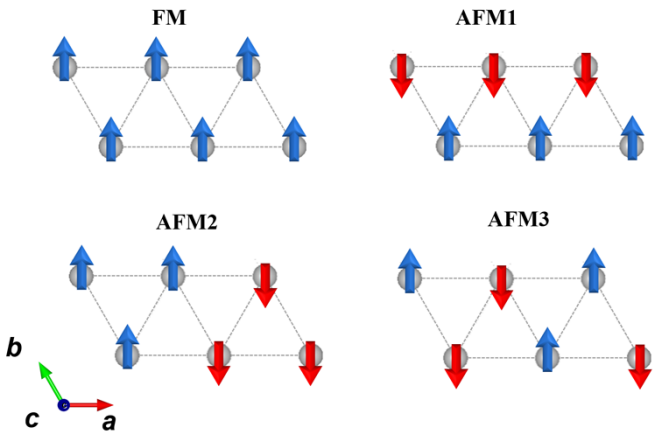

Fig. S3 Schematic top view of four possible magnetic configurations. Red and blue arrows represent spin-up and spin-down, respectively.

To acquire Heisenberg exchange interactions *J*, we employ a 3 × 2 × 1 supercell and calculate the total energies for four distinct possible magnetic configurations, as shown in Fig. S3. The total energy of each spin configurations can be described by Eq (1) in the main text as follows:

$E_{FM} = E_0 - (18J_1 + 18J_2 + 18J_3)\,S^2$,

$E_{AFM1} = E_0 - (-6J_1 - 6J_2 + 18J_3)\,S^2$,

$E_{AFM2} = E_0 - (-2J_1 - 6J_2 + 2J_3)\,S^2$,

$E_{AFM3} = E_0 - (-6J_1 + 2J_2 + 2J_3)\,S^2$.

Here, E_{FM}, E_{AFM1}, E_{AFM2} and E_{AFM3} are the energies of the supercell with the four possible magnetic configurations, which can be obtained from first-principles calculations. E_0 is a constant of non-magnetic section, which is not related to the spin of magnetic atoms. J_1, J_2 and J_3 are the Heisenberg exchange interactions of first, second and third nearest neighbors, respectively. Thus, J_1, J_2 and J_3 are extracted by:

$$J_1 = \frac{E_{FM}}{36} - \frac{E_{AFM1}}{36} + \frac{E_{AFM2}}{12} - \frac{E_{AFM3}}{12},$$

$$J_2 = \frac{E_{FM}}{72} - \frac{E_{AFM1}}{72} - \frac{E_{AFM2}}{12} + \frac{E_{AFM3}}{12},$$

$$J_3 = \frac{E_{FM}}{144} + \frac{E_{AFM1}}{18} - \frac{E_{AFM2}}{24} - \frac{E_{AFM3}}{48}.$$

Tab. S2. The specific Heisenberg exchange interaction *J* of NiI_2 monolayer under different strain ε (%).

ε (%)	-8	-6	-4	-2	0	2	4	6	8
J_1 (meV)	-1.94	-2.92	-3.54	-3.85	-3.94	-3.88	-3.72	-3.48	-3.20
J_2 (meV)	-1.02	-0.76	-0.59	-0.45	-0.36	-0.28	-0.23	-0.20	-0.17
J_3 (meV)	8.54	6.69	5.25	4.14	3.28	2.61	2.09	1.68	1.36
$\lvert J_3\rvert/J_1$	4.40	2.29	1.48	1.08	0.83	0.67	0.56	0.48	0.43

IV. Single ion anisotropy (SIA) energy and Orbital-resolved SIA

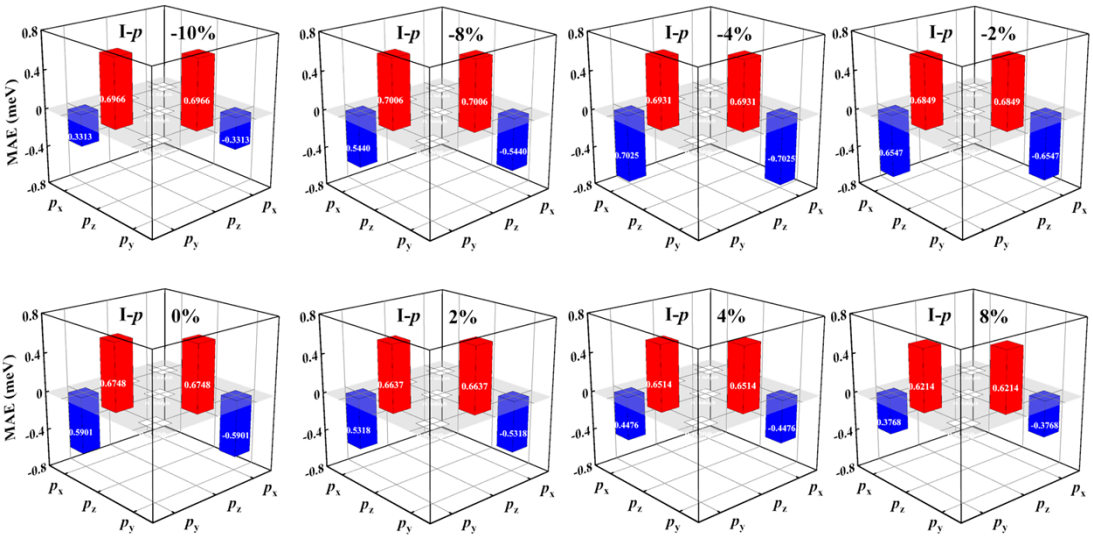

Fig. S4 The orbital-resolved SIA of I-p orbital under various strain ε.

The single ion anisotropy (SIA) energy A_i is defined as the energy difference between in-plane and out-of-plane magnetizations of a 1× 1 surface unit cell of NiI_2 monolayer with considering the SOC effect (SIA = E_{in}− E_{out}). A positive (negative) SIA value indicates ferromagnets having an out-of-plane (in-plane) spin polarization direction. According to the second-order perturbation theory[10], the contribution of each orbital pair to SIA can be described by spin-orbit-coupling matrix element differences and energy differences between the occupied and unoccupied states, i.e., $SIA \propto \xi^2 \sum_{o,u} \frac{|\langle p_o|\hat{L}_z|p_u\rangle|^2 - |\langle p_o|\hat{L}_x|p_u\rangle|^2}{E_u - E_o}$, where ξ represents the SOC amplitude; p_o and p_u indicate the occupied and unoccupied states of p orbital, respectively; $E_u - E_o$ is the energy difference between p_u and p_o states; $\hat{L}_x$ and $\hat{L}_z$ are the angular momentum operators along the $[100]$ and $[001]$ directions, respectively.

V. Choice of Hubbard-U value

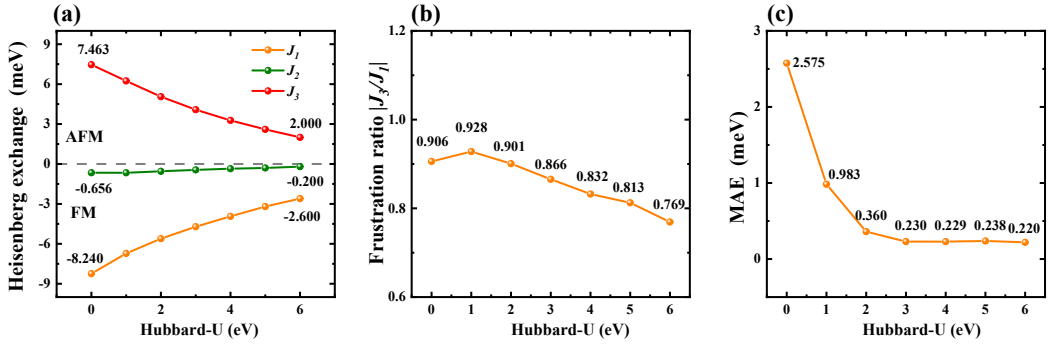

Fig. S5 (a) Heisenberg exchange interactions (b) frustration ratio $|J_3/J_1|$ and (c) magnetic anisotropy energy (MAE) as a function of the Hubbard-*U* parameter.

Additional calculations have been performed to test the robustness of our key magnetic exchange parameters. As shown in Fig. S5, we have systematically tested the sensitivity of the first-, second-, and third-nearest neighbors Heisenberg exchange interactions to the Hubbard-U value. The results show that while the absolute values of J vary with U_{eff}, their signs and, most importantly, the frustration ratio exhibits only a modest variation (decreasing from 0.93 to 0.77) across the whole range of U_{eff}, which dictates the minor effect of U_{eff} value on the magnetic frustration and the stability of the non-collinear spin spiral state. This confirms that our central conclusion about the spin spiral ground state is robust against small variations in the U parameter. Furthermore, the MAE shows a converged trend. While its value decreases from a large positive value (out-of-plane easy axis) at $U_{eff} = 0$ eV, it stabilizes around 0.23 meV for $U_{eff} \geq 3$ eV. Crucially, the sign of the MAE remains positive throughout the tested range, confirming that the out-of-plane easy axis is robust against the choice of U. This convergence strongly supports the reasonability of our chosen value of $U_{eff} = 4.0$ eV, as it lies well within this stable parameter region.

VI. Higher-order exchange interactions from DFT

The fourth-order perturbative expansion in the hopping parameter leads to the higher-order exchange interactions, which consists of two-site-four-spin interaction (biquadratic interaction, BQ), three-site-four-spin interaction (Y) and four-site-four-spin interaction (F). These terms arise due to hopping of the electron among two, three, and four lattice sites. To compute these three HOI constants, several multi-Q states need to be taken into account. The multi-Q state is constructed from the superposition of spin spirals (single-Q) related to symmetry equivalent q vectors of the 2DBZ. A linear combination of these two spirals will lead to a new spin configuration that is energetically degenerate in the Heisenberg model, while this degeneracy will be lifted by considering the higher-order interaction terms. A prominent example is the collinear uudd or double-row wise antiferromagnetic state originating from a superposition of two counterpropagating 90◦ spin spirals.

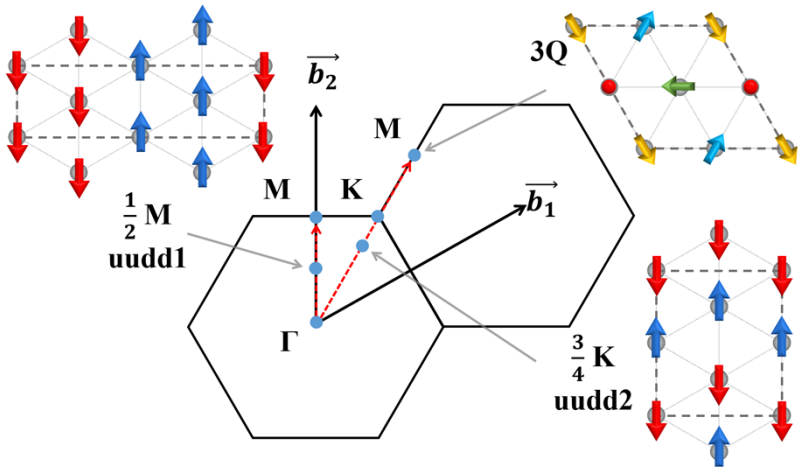

Fig. S6 (a) The sketch of 2D hexagonal Brillouin zone with the position of q vector and the magnetic order of the 2D collinear uudd states at $q = \frac{1}{2}$ M and $q = \frac{3}{4}$ K, as well as the 3D noncollinear 3q state.

Here, we consider two collinear states (namely, uudd1 state and uudd2 state) and a three-dimensional noncollinear state (*i.e.* 3Q state) to determine these three HOI constants. The two uudd states occur at q=M/2 and q=3K/4, which are corresponding to different high symmetry paths. While the 3Q state is located at M point, which is adopted in a 2*2 supercell with $S_1 = (0,0,1)$, $S_2 = \left(-\frac{2\sqrt{2}}{3}, 0, -\frac{1}{3}\right)$, $S_3 = \left(\frac{\sqrt{2}}{3}, -\frac{\sqrt{6}}{3}, -\frac{1}{3}\right)$ and $S_4 = \left(\frac{\sqrt{2}}{3}, \frac{\sqrt{6}}{3}, -\frac{1}{3}\right)$, as shown in Fig. S6. The three HOI

constants without SOC are determined from the energy differences between the single-Q and multi-Q states by solving the three coupled equations below:

$$\Delta E_{\left(uudd1-\frac{M}{2}\right)} = E_{uudd1} - E_{\frac{M}{2}} = \frac{16}{3}(2F + B - Y)$$

$$\Delta E_{\left(uudd2-\frac{3K}{4}\right)} = E_{uudd2} - E_{\frac{3K}{4}} = 4(2F - B - Y)$$

$$\Delta E_{(3Q-M)} = E_{3Q} - E_{M} = 4(2F - B + Y)$$

Therefore, the three HOIs can be expressed as:

$$B = \frac{3}{32}\Delta E_{(3Q-M)} - \frac{1}{8}\Delta E_{\left(uudd1-\frac{M}{2}\right)}$$

$$Y = \frac{1}{8}\Delta E_{\left(uudd2-\frac{3K}{4}\right)} - \frac{1}{8}\Delta E_{\left(uudd1-\frac{M}{2}\right)}$$

$$F = \frac{3}{64}\Delta E_{(3q-M)} + \frac{1}{16}\Delta E_{\left(uudd2-\frac{3K}{4}\right)}$$

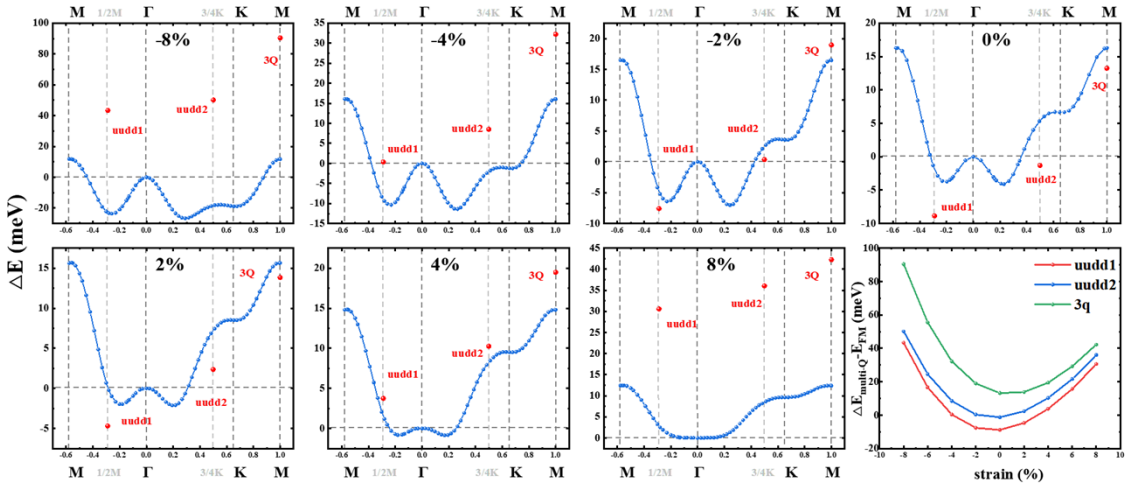

Fig. S7 Energy dispersion E(q) for ML-NiI_2 along two high symmetry directions without SOC under various biaxial strain. The red dots represent the energy of multi-Q (3Q and uudd) states, which are located at the q points (light gray vertical dotted line) of the corresponding single-Q states.

Note that in some case the uudd1 state has a lower energy, which is a definitive signature of substantial HOIs that energetically prefer collinear spin configurations over non-collinear ones. This phenomenon, recently highlighted in other frustrated magnets[11, 12], allows us to isolate and confirm the strength of HOIs. The actual magnetic ground state is determined by the interplay of all interactions without constraints; the frustrated Heisenberg exchange promotes the formation of a spin spiral, while the HOIs

suppress large-angle non-collinearity. Consequently, a stable and nearly collinear spiral state is resulted.

In addition, upon taking the higher-order exchange interactions into account, the energy dispersion relation up to 3rd NN for a hexagonal lattice with the q vector propagating along the Γ-K direction can be described as:

$$E_{(q)} = -[\cos(2\pi q) + 2\cos(\pi q)]\left(J_1^{'} + Y\right) - [1 + 2\cos(3\pi q)]\left(J_2^{'} + Y\right) - \left(J_3^{'} + \frac{B}{2}\right) - 12F$$

Therefore, the first three Heisenberg exchange interaction needs to be modified as follows:

$$J_1^{'} = J_1 - Y$$

$$J_2^{'} = J_2 - Y$$

$$J_3^{'} = J_3 - \frac{B}{2}$$

Here, the J_1, J_2 and J_3 are Heisenberg exchange interaction in Tab. S2 obtained by the energy difference method. Note that the contribution of the four-site-four-spin interaction F to the energy dispersion of spin spirals is a constant value of $-12F$ independent of the spin spiral vector and therefore F does not affect any exchange interaction parameters.

VII. Specific values of magnetic exchange parameters

Tab. S3 The Heisenberg exchange interactions under various biaxial strains. The *B*, *Y* and *F* represent biquadratic, three-site-four-spin and four-site-four-spin interactions for ML-NiI_2, respectively. The modified and unmodified Heisenberg exchange interactions are denoted as $\boldsymbol{J_i}'$ and $\boldsymbol{J_i}$, respectively. The exchange parameters are modified upon including the higher-order interactions. All exchange interaction values are given in meV. The $|J_3|/J_1$ represents frustration ratio.

Strain (%)	$J_1(J_1')$	$J_2(J_2')$	$J_3(J_3')$	$\lvert J_3\rvert/J_1$ $\lvert J_3'\rvert/J_1'$	*B*	*Y*	*F*
-8	-1.94	-1.02	8.54	4.40	0.00	0.00	0.00
	-2.15	-1.23	9.02	4.20	-0.96	0.21	7.95
-6	-2.92	-0.76	6.69	2.29	0.00	0.00	0.00
	-3.08	-0.92	6.76	2.19	-0.14	0.16	3.98
-4	-3.54	-0.59	5.25	1.48	0.00	0.00	0.00
	-3.60	-0.65	5.10	1.42	0.30	0.06	1.40
-2	-3.85	-0.45	4.14	1.08	0.00	0.00	0.00
	-3.85	-0.45	3.87	1.01	0.53	0.00	-0.03
0	-3.94	-0.36	3.28	0.83	0.00	0.00	0.00
	-3.93	-0.35	3.01	0.77	0.54	-0.01	-0.56
2	-3.88	-0.28	2.61	0.67	0.00	0.00	0.00
	-3.81	-0.21	2.41	0.63	0.39	-0.07	-0.40
4	-3.72	-0.23	2.09	0.56	0.00	0.00	0.00
	-3.62	-0.13	2.03	0.56	0.12	-0.10	0.33
6	-3.48	-0.20	1.68	0.48	0.00	0.00	0.00
	-3.39	-0.11	1.80	0.53	-0.24	-0.09	1.53
8	-3.20	-0.17	1.36	0.43	0.00	0.00	0.00
	-3.12	-0.09	1.71	0.55	-0.71	-0.08	3.11

VIII. Estimation of Dzyaloshinskii-Moriya interaction (DMI)

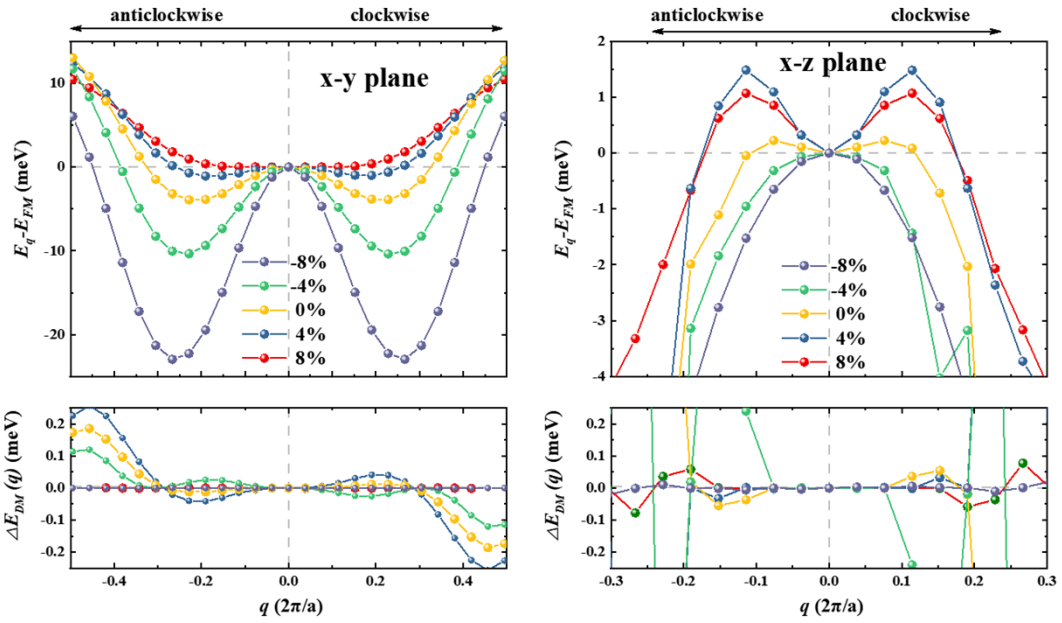

Fig. S8 Calculated SOC-included spin spiral energy E(q) rotating in (a) x-y plane and (b) x-z plane and their corresponding DMI energy $\Delta E_{DM\ (q)}$ as a function of spiral vector length q along Γ-K direction. E(q) is given with respect to the ferromagnetic state at q=0.

The Dzyaloshinskii-Moriya interaction (DMI) is essentially magnetic interaction caused by spin-orbit coupling (SOC) and breaking of spatial inversion symmetry, which can be expressed as $\vec{d}_{ij} = d_{//}(\vec{u}_{ij} \times \vec{z}) + d_{\perp}\vec{z}$. Here, $\vec{u}_{ij}$ and $\vec{z}$ are the unit vectors from site *i* to site *j* and along the *z* direction, respectively. Due to the existence of inversion symmetry in ML-NiI_2, it is expected that there is no DMI. To verify that DMI of ML-NiI_2 is zero, we estimate the two components ($d_{//}$ and $d_{\perp}$.) of the DMI by considering SOC-included spin spirals rotating in the x-y plane and x-z plane based on first-order perturbation of generalized Bloch theorem. The energy dispersion *E(q)* with the spin spiral in x-y plane and x-z plane are shown in the upper panels of Fig. S8. The DMI energy are determined by $E_{DM}(q) = [E(q) - E(-q)]/2$, and the DMI can be extracted from the slope of the energy contribution close to q= 0, as shown in the lower panels. In small q region with $|q| < 0.05$ (2π/a), the slopes of $\Delta E_{DM}(q)$ become infinitesimal, which indicates that the d values equal zero for both $d_{//}$ and $d_{\perp}$.

Critically, we also extend these calculations to the strained systems (e.g., ±8% biaxial strain) and find the same result, i.e., the DMI remains zero. This provides definitive evidence that the net DMI remains zero and, consequently, the inversion

symmetry is maintained under all investigated strain conditions. Therefore, the stabilization of magnetic skyrmions and anti-skyrmions can be attributed exclusively to the strain-tuned symmetric higher-order interactions and magnetic frustration, as detailed in the main text.

IX. Negative integrated crystal Hamilton population (-ICOHP) for J_3

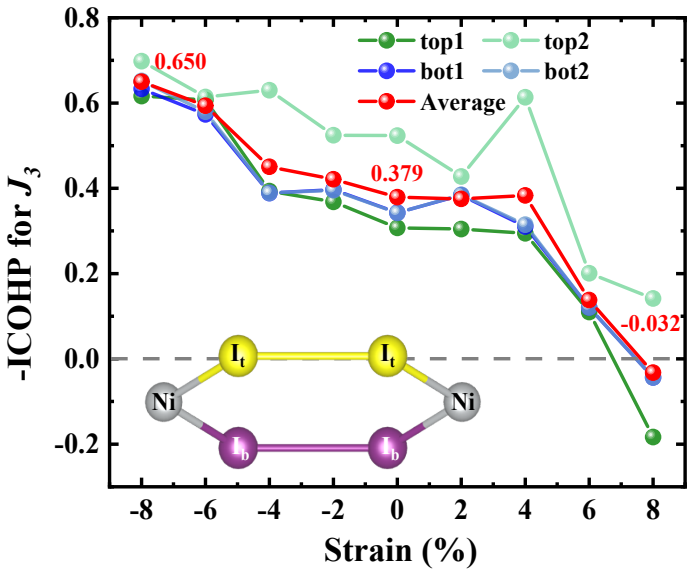

Fig. S9 The evolution of negative integrated crystal Hamilton population (-ICOHP) under the biaxial strain in ML-NiI_2.

X. Magnetic transition temperature and thermal stability

We perform classical Monte Carlo (MC) simulations to estimate the magnetic transition temperature of monolayer NiI_2 under different strain conditions. Here a 64×64×1 supercell is adopted. For each temperature point, the MC simulations involve 5×10^4 sweeps to sufficiently thermalize the system into equilibrium state, and the next 5×10^5 sweeps per site for acquiring the statistical results. The transition temperature is determined from the temperature dependence of magnetization and susceptibility. At 0% strain, the transition temperature is approximately 20 K, in good agreement with previous reports of 21 K[13] and 22.81 K[14]. While at 8% tensile strain it is reduced to about 10.9 K, again consistent with the reported value of 10.46 K[14].

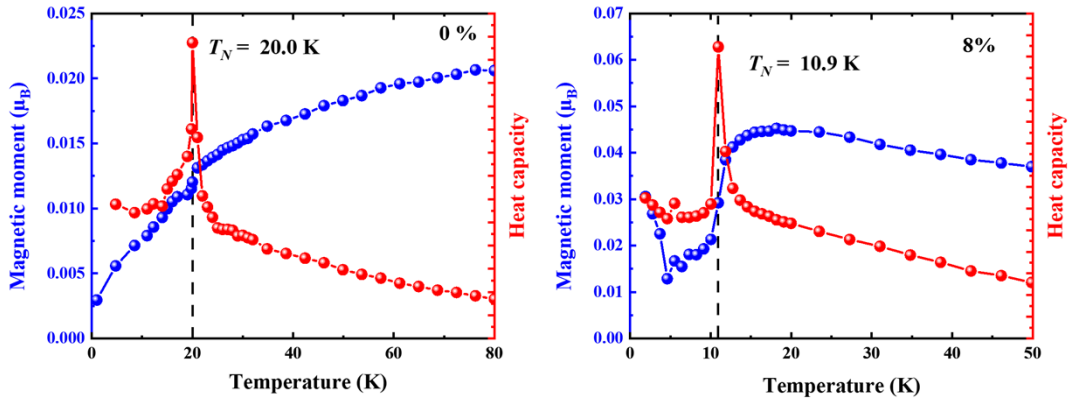

Fig. S10. The Monte Carlo simulations of magnetic moment and heat capacity as functions of temperature for ML-NiI_2 under 0% and 8% biaxial strain.

Additional spin-dynamics simulations at finite temperatures are carried out to examine the thermal stability of skyrmions. As shown in Fig. S11, thermal fluctuations progressively destabilize the skyrmions (and anti-skyrmions), which become metastable, while their qualitative behavior is consistent with the zero-temperature results. And the skyrmions (and anti-skyrmions) eventually disappear when the temperature approaches ~11 K, where the system enters a disordered phase. This critical temperature is fully consistent with the low transition temperature obtained from Monte Carlo simulations.

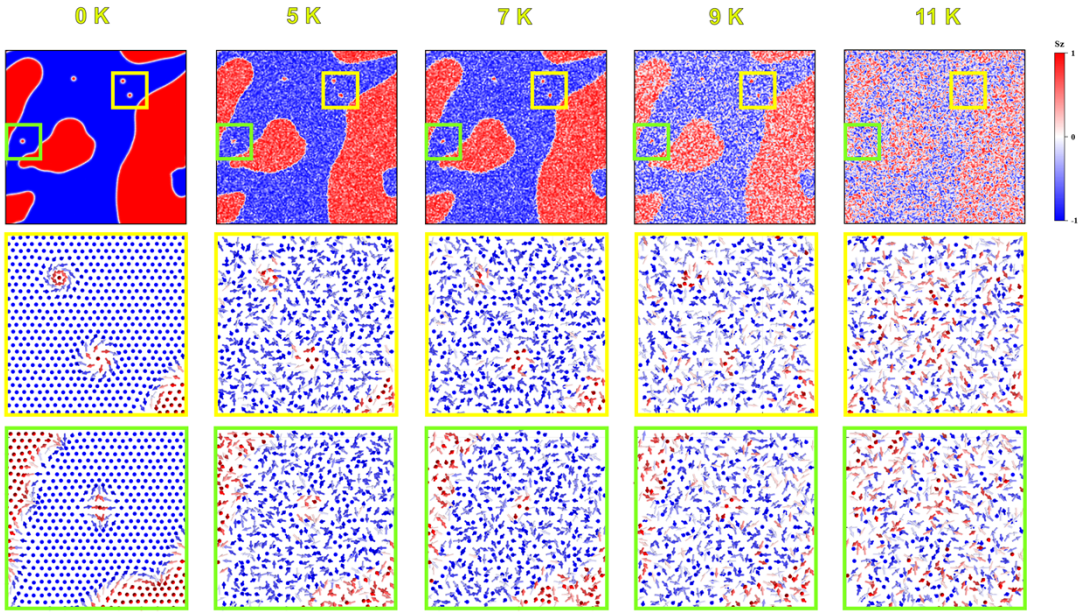

Fig. S11. Evolution of spin texture of ML-NiI_2 at 8% strain under different temperatures, considering all magnetic interactions included in Fig. 4(o) of the main text. The top row shows the spin textures in a simulation cell of 55 nm × 55 nm. The middle and bottom rows display enlarged views (10 nm × 10 nm) of the regions marked by the yellow and light-green squares in the top row, respectively.

XI. Finite-size convergence tests

To assess the impact of simulation cell size on the magnetic textures, we perform additional calculations using a significantly larger system size of 100 nm × 100 nm, compared to the 55 nm × 55 nm system employed in the main text. All simulations are conducted under +8% biaxial tensile strain and include the full set of magnetic interactions, namely the Heisenberg exchange (J), biquadratic interaction (B), and four-site four-spin exchange (F). As shown in Fig. S12, the main panel displays the full simulation region, while the three subpanels present enlarged views (10 nm × 10 nm) of selected regions marked by orange squares. Clear coexistence of skyrmions and antiskyrmions with characteristic diameters of approximately 2 nm is observed, consistent with the results reported in the main text.

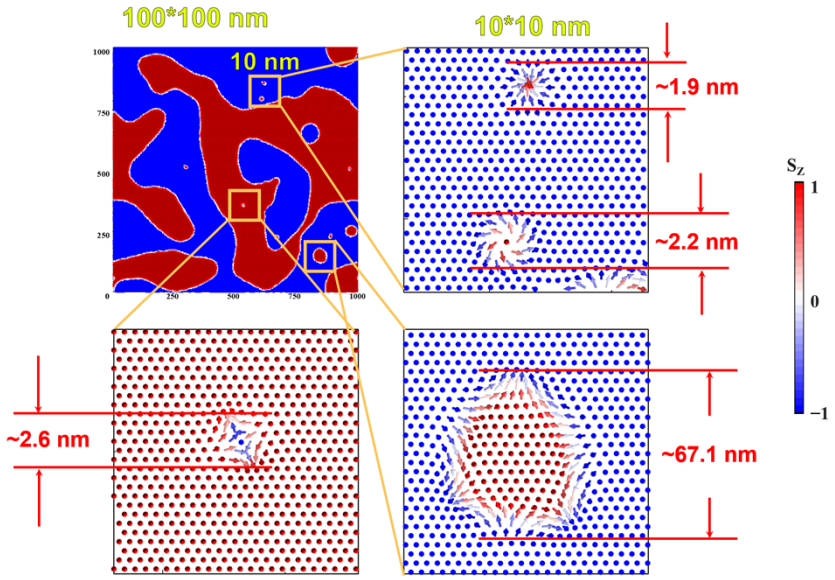

Fig. S12. Magnetic field-free spin textures of ML-NiI_2 under +8% biaxial strain, considering the full interplay between Heisenberg exchange (J), biquadratic interaction (B), and four-site-four-spin exchange (F). The main panel shows a 100 nm × 100 nm simulation region. The other three panels are enlarged views (10 nm × 10 nm each) of the areas marked by orange squares. The arrows indicate the orientation of in-plane spin component, and color bar indicates the out-of-plane spin component.

Fig. S13 further presents the evolution of spin textures under external magnetic fields. The qualitative response of the system to magnetic fields remains unchanged compared to the smaller system, demonstrating robust size convergence.

These results demonstrate that the 55 nm × 55 nm simulation cell adopted in the main text represents a balanced choice between computational efficiency and physical reliability, and is sufficient to capture the intrinsic coexistence behavior of skyrmions and antiskyrmions.

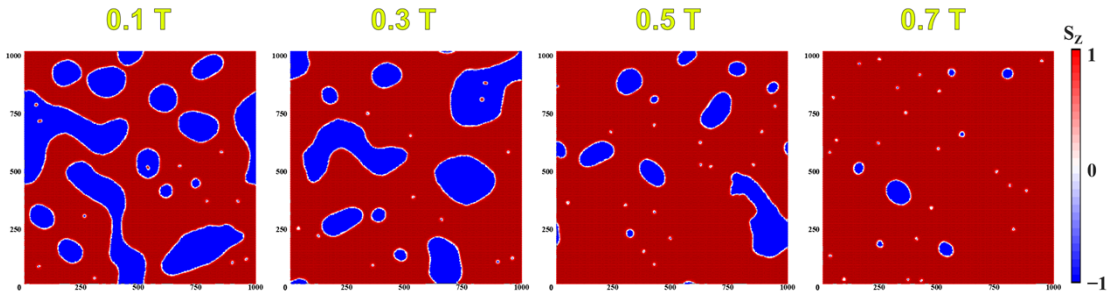

Fig. S13. Magnetic field-dependent spin textures in ML-NiI_2 under +8% strain with all higher-order interactions.

XII. Influence of the Kitaev Interaction on Spin Textures

To investigate the influence of Kitaev interaction on spin textures, we explicitly include the nearest-neighbor Kitaev interaction K in the spin Hamiltonian. Representative values of K are chosen based on recent literature for monolayer NiI_2[15], which reports *K* in the range of approximately −0.33 J_1 to −0.17 J_1. Using the nearest-neighbor Heisenberg exchange $J_1 \approx -3.12$ meV (at 8% strain) extracted from our first-principles calculations, four values are tested: K ≈ 0.53 meV (−0.17 J_1), 0.62 meV (−0.20 J_1), 0.78 meV (−0.25 J_1), and 1.03 meV (−0.33J_1). This range is consistent with values commonly reported for Ni-based halide systems[16].

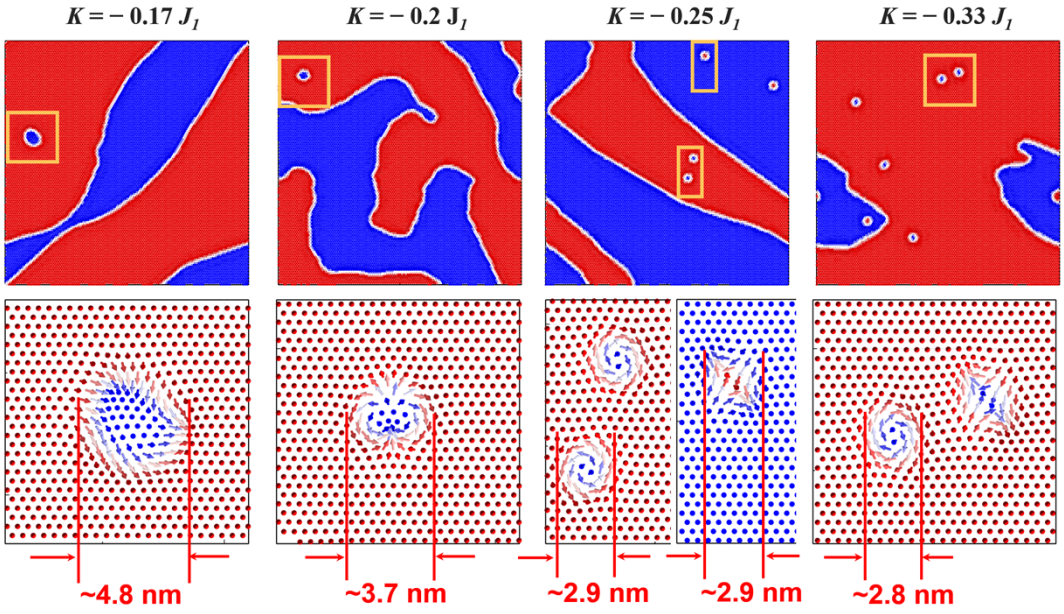

Fig. S14. Micromagnetic spin textures of monolayer NiI_2 obtained from atomistic simulations for four different Kitaev interaction strengths. The upper panels show the spin configurations in a 55 nm × 55 nm simulation cell, while the lower panels present enlarged views of the regions highlighted by yellow squares in the corresponding upper panels, with a size of 10 nm ×10nm.

Fig. S14 presents the micromagnetic spin textures obtained from atomistic simulations for the four K values. Across all tested K values, ultra-small skyrmions persist with characteristic sizes of a few nanometers. Increasing the Kitaev interaction leads to quantitative modifications, such as higher skyrmion density and slightly reduced size. Notably, at K = −0.25 J_1, a stable coexistence of skyrmions and antiskyrmions is observed, qualitatively consistent with the representative phase reported in the main text.

These results indicate that while the Kitaev term can fine-tune the spin textures, the fundamental mechanism stabilizing ultra-small skyrmions and antiskyrmions remains dominated by strain-enhanced higher-order interactions (HOIs). Therefore, the essential conclusions of the main text are not changed by inclusion of the Kitaev interaction, which acts primarily as a secondary, quantitative tuning parameter.

Reference

1. Sandratskii, L. M. *Phys. Status Solidi B* **1986,** 136, (1), 167-180.
2. Sandratskii, L. M. *J. Phys.: Condens. Matter* **1991,** 3, (44), 8565.
3. Sandratskii, L. M. *J Phys.: Condens. Matter* **1991,** 3, (44), 8587.
4. Kurz, P.; Förster, F.; Nordström, L.; Bihlmayer, G.; Blügel, S. *Phys. Rev. B* **2004,** 69, (2), 024415.
5. Kresse, G.; Furthmüller, J. *Phys. Rev. B* **1996,** 54, (16), 11169-11186.
6. Landau, L.; Lifshitz, E., 3 - On the theory of the dispersion of magnetic permeability in ferromagnetic bodies Reprinted from Physikalische Zeitschrift der Sowjetunion 8, Part 2, 153, 1935. In *Perspectives in Theoretical Physics*, Pitaevski, L. P., Ed. Pergamon: Amsterdam, 1992; pp 51-65.
7. Gilbert, T. L. *IEEE Transactions on Magnetics* **2004,** 40, (6), 3443-3449.
8. Evans, R. F. L.; Fan, W. J.; Chureemart, P.; Ostler, T. A.; Ellis, M. O. A.; Chantrell, R. W. *J. Phys.: Condens. Matter* **2014,** 26, (10), 103202.
9. Hoffmann, M.; Blügel, S. *Phys. Rev. B* **2020,** 101, (2), 024418.
10. Wang, D.-s.; Wu, R.; Freeman, A. J. *Phys. Rev. B* **1993,** 47, (22), 14932-14947.
11. Nickel, F.; Kubetzka, A.; Gutzeit, M.; Wiesendanger, R.; von Bergmann, K.; Heinze, S. *npj Spintronics* **2025,** 3, (1), 7.
12. Gutzeit, M.; Kubetzka, A.; Haldar, S.; Pralow, H.; Goerzen, M. A.; Wiesendanger, R.; Heinze, S.; von Bergmann, K. *Nature Communications* **2022,** 13, (1), 5764.
13. Song, Q.; Occhialini, C. A.; Ergeçen, E.; Ilyas, B.; Amoroso, D.; Barone, P.; Kapeghian, J.; Watanabe, K.; Taniguchi, T.; Botana, A. S.; Picozzi, S.; Gedik, N.; Comin, R. *Nature* **2022,** 602, (7898), 601-605.
14. Ni, X.-s.; Yao, D.-X.; Cao, K. *J. Magn. Magn. Mater.* **2025,** 613, 172661.
15. Li, X.; Xu, C.; Liu, B.; Li, X.; Bellaiche, L.; Xiang, H. *Phys. Rev. Lett.* **2023,** 131, (3), 036701.
16. Li, L.; Zhang, B.; Chen, Z.; Xu, C.; Xiang, H. *Phys. Rev. B* **2024,** 110, (21), 214435.